Principle and results of microwave diversity imaging of conducting objects using multisource illumination

C.-H. Tseng and T.-H. Chu

Abstract: The principle, measurement system, calibration and experimental results of microwave diversity imaging of conducting objects in a multisource illumination arrangement are presented. Theoretical analysis is developed under multiple plane wave illumination and physical optics approximation. The measurement system and calibration procedure are implemented based on plane wave spectrum analysis. Reconstructed images of four different types of conducting objects, including continuous shape and discrete line objects, measured in the frequency range 7.5–12.5 GHz, are shown in good agreement with the scattering object geometries. The experimental results demonstrate that the developed microwave imaging system is an effective approach to yield microwave images of scattering objects with a wide aspect angle.

1 Introduction

Microwave imaging is an approach to reconstructing the scattering object characteristics from the recorded object scattered field in the microwave frequency range [1, 2]. It finds applications in imaging radar [3–5], remote sensing [6], nondestructive evaluation [7, 8], antenna [9, 10], biological diagnoses [11, 12], target identification [13], etc., because microwaves can penetrate fog, cloud and a variety of dielectric materials. In general, high resolution and wide aspect angle are the main design requirements of a microwave imaging system. Therefore, it is essential to acquire enough object scattering information at different frequencies, receiving and illumination angles.

For the microwave imaging of conducting objects, frequency and receiving angle diversity techniques have been applied in the bistatic arrangement [14]. In this arrangement, the scattering object is at a fixed location and the frequency-swept object scattering information at different receiving angles is recorded by a linear receiving array. These diversity techniques are shown to yield good image resolution by effectively extending the recorded object scattering information in the Fourier domain. Similarly, the time-domain ultrawideband microwave imaging system has been shown to be able to obtain high-resolution images [15, 16].

In this paper, we extend the bistatic frequency-swept microwave imaging system in [14] for single-source illumination to the case of multisource illumination. In other words, the scattering object is under the illumination of multiple sources to give a larger illuminated region on the object surface. The scattered field is recorded by a linear array in a backward scattering arrangement. The reconstructed image then gives an image corresponding to the induced surface current distribution on the illuminated region owing to the specular diffraction observed by the linear receiving array. As a result, the multisource illumination will enlarge the illuminated region on the scattering object surface, hence improving the resulting image aspect angle.

In Section 2, the formulations for image reconstruction of conducting objects for multisource illumination are presented. Since the scattering object is illuminated by multiple sources, the induced currents contributed from each illuminating source then interfere with each other on the object surface. The recorded object scattered field is therefore a coherent summation of the scattered fields from the illuminated regions. In this paper, an image reconstruction method is developed to use sets of equations in the Fourier domain to solve the corresponding portion of scattered field contributed from each illumination source.

The developed microwave imaging system and calibration procedure for multisource illumination are described in Section 3. In the measurement system, an open-ended rectangular waveguide probe is mounted on a linear scanner to simulate the linear receiving array. The mutual coupling effect in the linear array is therefore not considered in this arrangement. In the measurement, the receiving probe response is calibrated for acquiring the object Fourier-domain data. Formulations in this Section describe the relationship between the Fourier-domain data of the measured scattered field and the calibrated portion of Fourier-domain data contributed from each illumination source.

In Section 4, images reconstructed from the experimental data for four different types of scattering objects show that the developed microwave diversity imaging system, using multisource illumination, is capable of achieving images with a wide aspect of the scattering object.

2 Principle

The purpose of this Section is to develop the basic formulation of microwave diversity imaging of conducting objects with multisource illumination. Figure 1 shows the scattering geometry with multisource illumination and a backward linear receiving array. In the following derivation,

---

IEE Proceedings online no. 20040179

doi:10.1049/ip-map:20040179

Paper first received 27th January and in revised form 29th September 2003. Online publishing date: 19 February 2004

The authors are with the Graduate Institute of Communication Engineering, National Taiwan University, No. 1, Sec. 4, Roosevelt Road, Taipei, Taiwan 106, R.O.C.

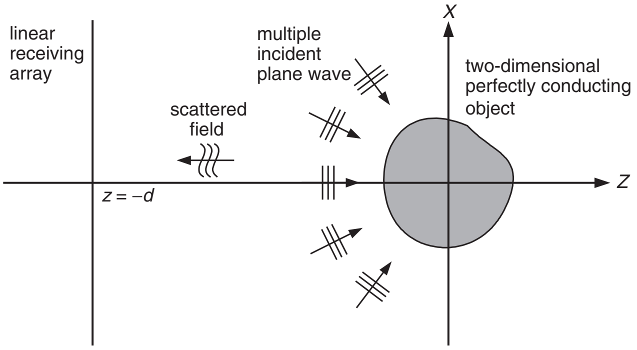

Fig. 1 *Two-dimensional scattering geometry with multisource illumination*

an infinitely long scattering object in the y-direction (normal to the x–z plane) is assumed and illuminated by multiple normally incident TM-polarised plane waves.

The incident field for multisource illumination is written as

$$\begin{aligned} \boldsymbol{E}^i(\boldsymbol{r}) &= \hat{y}E_1 e^{-jk_0\hat{k}_1\cdot\boldsymbol{r}} + \hat{y}E_2 e^{-jk_0\hat{k}_2\cdot\boldsymbol{r}} + \cdots \\ &\quad + \hat{y}E_n e^{-jk_0\hat{k}_n\cdot\boldsymbol{r}} \\ &= \hat{y}\sum_{i=1}^{n} E_i e^{-jk_0\hat{k}_i\cdot\boldsymbol{r}} \end{aligned} \tag{1}$$

$$\boldsymbol{H}^i(\boldsymbol{r}) = \frac{1}{\eta}\sum_{i=1}^{n} \hat{k}_i \times \hat{y}E_i e^{-jk_0\hat{k}_i\cdot\boldsymbol{r}} \tag{2}$$

where $k_0 = \omega/c$ is the wave number and $\hat{k}_i$ is the direction of the ith incident plane wave. E_i is the complex field amplitude of the ith incident plane wave. η is the intrinsic impedance in free space and $\exp(jwt)$ time dependence is implied.

Based on [14], the scattered field recorded by the linear receiving array at $z = -d$ can be represented as

$$\begin{aligned} &U^s(x, z = -d, k_0) \\ &\quad = \kappa\sum_{i=1}^{n} E_i \iint O_i(\boldsymbol{r}')e^{-jk_0\hat{k}_i\cdot\vec{r}'}G(|\boldsymbol{r}-\boldsymbol{r}'|)d^2\boldsymbol{r}' \end{aligned} \tag{3}$$

where $\kappa = -jk_0$ for the continuous scattering object and $\kappa = 1$ for the discrete scattering object. $O_i(\boldsymbol{r}')$ is defined as the ith portion of the object function contributed from the ith source illumination.

$$G(|\boldsymbol{r}-\boldsymbol{r}'|) = \frac{1}{4j}H_0^{(2)}(k_0|\boldsymbol{r}-\boldsymbol{r}'|) \tag{4}$$

is the Green's function in free space [17].

By using the wave expansion of the Green's function [18]

$$G(|\boldsymbol{r}-\boldsymbol{r}'|) = \frac{1}{2\pi}\int \frac{-j}{2\gamma}e^{-j[\gamma|-d-z'|+k_x(x-x')]}dk_x \tag{5}$$

where $\boldsymbol{r} = x\hat{x} - d\hat{z},\ \boldsymbol{r} = x'\hat{x} + z'\hat{z}$

$$\gamma = \sqrt{k_0^2 - k_x^2}\ \text{as}\ |k_x| \le k_0 \tag{6}$$

and performing a one-dimensional Fourier transform, one can obtain

$$\tilde{U}^s(k_x, z = -d, k_0) = \frac{-j\kappa}{2\gamma}e^{-j\gamma d}\sum_{i=1}^{n} E_i\tilde{O}_i(k_x, -\gamma, -k_0) \tag{7}$$

In (7), the Fourier transformation of the scattered field $U^s(x, z = -d, k_0)$ and the object function $O(\boldsymbol{r})$ are defined as

$$\tilde{U}^s(k_x, z = -d, k_0) = \int U^s(x, z = -d, k_0)e^{jk_x x}dx \tag{8}$$

$$\tilde{O}(\boldsymbol{k}) = \iint O(\boldsymbol{r})e^{j\boldsymbol{k}\cdot\boldsymbol{r}}d^2\boldsymbol{r} \tag{9}$$

$\boldsymbol{k} = k_x\hat{x} + k_z\hat{z}$ is the wave vector in Fourier-domain space, and is expressed as

$$(k_x + k_0\sin\theta_i)^2 + (k_z + k_0\cos\theta_i)^2 = k_0^2 \tag{10}$$

where θ_i is the angle between the direction of the ith incident plane wave and z-axis. One can then define the microwave image of the scattering object to be the intensity of the corresponding object function as $|O(\boldsymbol{r})|^2$.

In order to relate the reconstructed microwave image to the Fourier transformation of the scattered field given in (7), the corresponding Fourier-domain data contributed from each illumination source has to be extracted. By rewriting the amplitude E_i in (1) as E_{ij} with $i, j = 1\ \ldots\ n$, one can expand (7) to be a set of n equations as

$$\begin{aligned} \tilde{U}_1^s &= \frac{-j\kappa}{2\gamma}e^{-j\gamma d}[E_{11}\tilde{O}_1 + E_{12}\tilde{O}_2 + \cdots + E_{1n}\tilde{O}_n] \\ \tilde{U}_2^s &= \frac{-j\kappa}{2\gamma}e^{-j\gamma d}[E_{21}\tilde{O}_1 + E_{22}\tilde{O}_2 + \cdots + E_{2n}\tilde{O}_n] \\ &\vdots \\ \tilde{U}_n^s &= \frac{-j\kappa}{2\gamma}e^{-j\gamma d}[E_{n1}\tilde{O}_1 + E_{n2}\tilde{O}_2 + \cdots + E_{nn}\tilde{O}_n] \end{aligned} \tag{11}$$

In (11), amplitudes of E_{ij} are properly assigned to yield n linearly independent equations and each equation is considered as a measurement state. In other words, during the measurement to be described in the following Section, the amplitudes of n multisources are properly arranged for a total of n measurement states.

Equation (11) can then be expressed as

$$\begin{bmatrix} \tilde{O}_1 \\ \tilde{O}_2 \\ \vdots \\ \tilde{O}_n \end{bmatrix} = \frac{j2\gamma}{\kappa}e^{j\gamma d}\begin{bmatrix} E_{11} & E_{12} & \cdots & E_{1n} \\ E_{21} & E_{22} & \cdots & E_{2n} \\ \vdots & \vdots & \ddots & \vdots \\ E_{n1} & E_{n2} & \cdots & E_{nn} \end{bmatrix}^{-1}\begin{bmatrix} \tilde{U}_1^s \\ \tilde{U}_2^s \\ \vdots \\ \tilde{U}_n^s \end{bmatrix} \tag{12}$$

or

$$[\tilde{O}_i] = \frac{j2\gamma}{\kappa}e^{j\gamma d}[\boldsymbol{E_{ij}}]^{-1}[\tilde{U}_j^s] \tag{13}$$

Equation (12) shows that results of $\tilde{O}_i$ corresponding to the ith illumination source can be extracted from the scattered field $\tilde{U}^s$ in the Fourier domain with a known nonsingular matrix $[\boldsymbol{E_{ij}}]$. Therefore, by superposing all the Fourier-domain data and performing two-dimensional inverse FFT (fast Fourier transformation), a microwave image with a wider aspect angle can be achieved than that for single-source illumination arrangement in [14], since its Fourier domain is enlarged by using multisource illumination. This result will be shown in Section 4.

In the developed measurement system, the amplitudes of $\boldsymbol{E_{ij}}$ for the multiple sources are electrically controlled by step attenuators and the scattered field for all the measurement states are recorded automatically at each receiving antenna position. Hence, it becomes a more effective approach to yield images with a wide aspect angle compared to the approach of single illumination. In the following Section, the experimental measurement system and its calibration procedure to acquire the scattering object Fourier-domain data will be described.

3 Measurement system and calibration procedure

Figure 2 shows the developed microwave imaging measurement system. In order to give a proper illumination

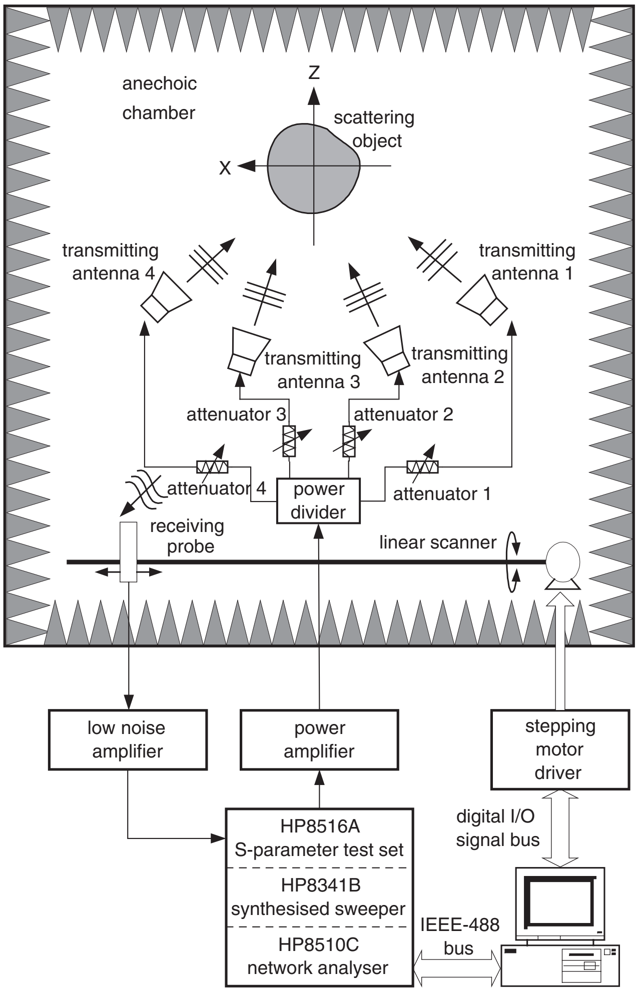

Fig. 2 *Automated wide-band scattering measurement system with four-source illumination*

coverage over the scattering object, it has four transmitting horn antennas at about 60°, 30°, −30° and −60° to simulate four-source illumination. Their power levels are controlled by four attenuators. An open-ended WR-90 waveguide is used as a receiving probe, located on a 158 cm long linear scanner at about $z = -40$ cm to collect the object scattered field. A Hughes 8010 H travelling wave tube amplifier (TWTA) and an Avantek AWT-18676 low noise amplifier (LNA) are connected with an HP8510C network analyser to provide proper signal amplification. A personal computer is linked to the measurement system for receiving probe movement, instrument control, system calibration and data recording.

In the measurement, the four attenuators are electronically set to be 3 dB in turn to give four measurement states. The other three attenuators in each measurement state are set to be 0 dB. One measurement state is meant to record the frequency-swept object scattered field for one set of attenuator values. The measurement sequence is first to perform four measurement states, then the receiving probe is moved to the next position for the next four measurement states until the end of the scanner. The frequency responses of attenuators at each setting value are measured before the experiment. Note the consideration in choosing attenuator setting values is to give a nonsingular matrix $[\boldsymbol{E_{ij}}]^{-1}$ in (13), hence one may select other values. In addition, since the attenuators are calibrated, their setting values will not affect the measurement performance.

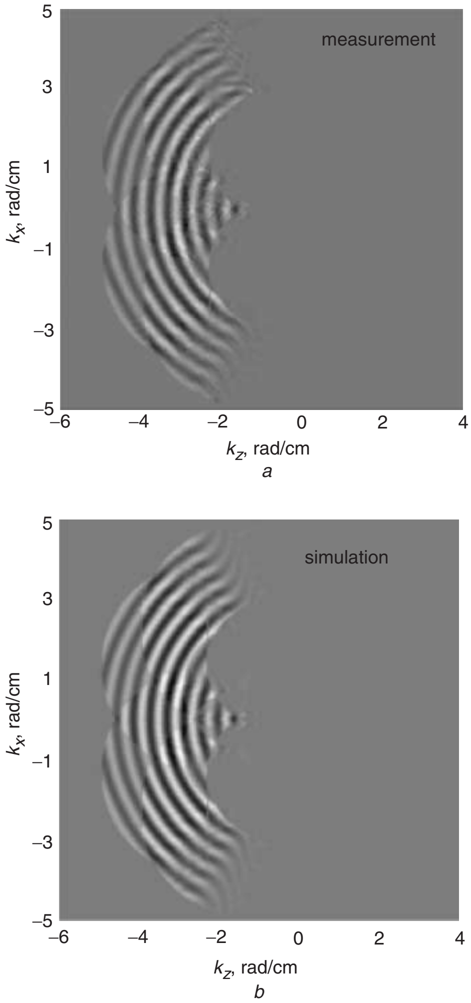

a

b

Fig. 3 *Fourier-domain data of a metallic cylinder with radius $a = 15$ cm under four-source illumination*
a Measurement results
b Simulation results

Based on the calibration procedure of the single-source illumination arrangement [14] and the plane wave spectrum (PWS) technique [19], the calibration procedure for the measurement system given in Fig. 2 is described in the following.

In practice, the measured scattered field in the Fourier domain can be represented as

$$[\tilde{U}_j^m] = [\tilde{I}_j]e^{-j\gamma d} + \frac{-j\kappa}{2\gamma} e^{-j\gamma d}[E_{ij}][\tilde{O}_i\tilde{R}_j] \tag{14}$$

$\tilde{I}_j$ is the room clutter term in the jth measurement state and it is directly obtained by one-dimensional Fourier transformation of the measured signal without locating any scattering object inside the anechoic chamber. $[\boldsymbol{E_{ij}}]$ is an $n \times n$ nonsingular matrix to account for the different complex amplitudes of multi-incident plane waves in the jth measurement state. $\tilde{O}_i\tilde{R}_j$ is the product of the ith portion of Fourier-domain data and system frequency response in the jth measurement state. Equation (14) can be rewritten as

$$[\tilde{O}_i\tilde{R}_j] = \frac{j2\gamma}{\kappa} e^{j\gamma d}[\tilde{X}_i] \tag{15}$$

where

$$[\tilde{X}_i] = [\boldsymbol{E_{ij}}]^{-1}\{[\tilde{U}_i^m] - [\tilde{I}_j]e^{-j\gamma d}\} \tag{16}$$

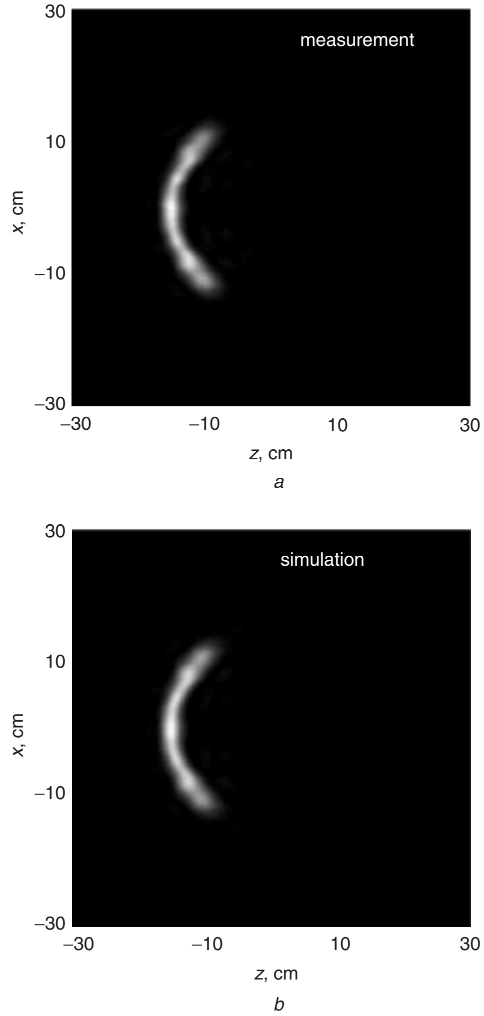

Fig. 4 *Reconstructed images of a metallic cylinder with radius a = 15 cm obtained from Fourier-domain data given in Fig. 3*
a Measurement results
b Simulation results

For a reference scattering object, (14) becomes

$$[\tilde{U}_j^{ref}] = [\tilde{I}_j]\, e^{-j\gamma d} + \frac{-jk}{2\gamma} e^{-j\gamma d} [\boldsymbol{E_{ij}}]\, [\tilde{O}_i^{ref} \tilde{R}_j] \tag{17}$$

$\tilde{U}_j^{ref}$ is the measured Fourier-domain data in the *j*th measurement state and $\tilde{O}_i^{ref}$ is the calculated Fourier-domain data of the reference object contributed from the *i*th illumination source. (17) can be represented as

$$[\tilde{O}_i^{ref} \tilde{R}_j] = \frac{j2\gamma}{\kappa} e^{j\gamma d} [\tilde{Y}_i] \tag{18}$$

where

$$[\tilde{Y}_i] = [\boldsymbol{E_{ij}}]^{-1} \{[\tilde{U}_j^{ref}] - [\tilde{I}_j] e^{-j\gamma d}\} \tag{19}$$

Therefore, the system frequency response of the *j*th measurement state can be eliminated by dividing $\tilde{O}_i \tilde{R}_j$ in (15) by $\tilde{O}_i^{ref} \tilde{R}_j$ in (18) to acquire the calibrated *i*th portion of the Fourier-domain data as

$$\tilde{O}_i = \frac{\tilde{X}_i}{\tilde{Y}_i} \tilde{O}_i^{ref} \tag{20}$$

Based on the calibration equations (18) and (20), the calibration and measurement procedures are summarised as the following:

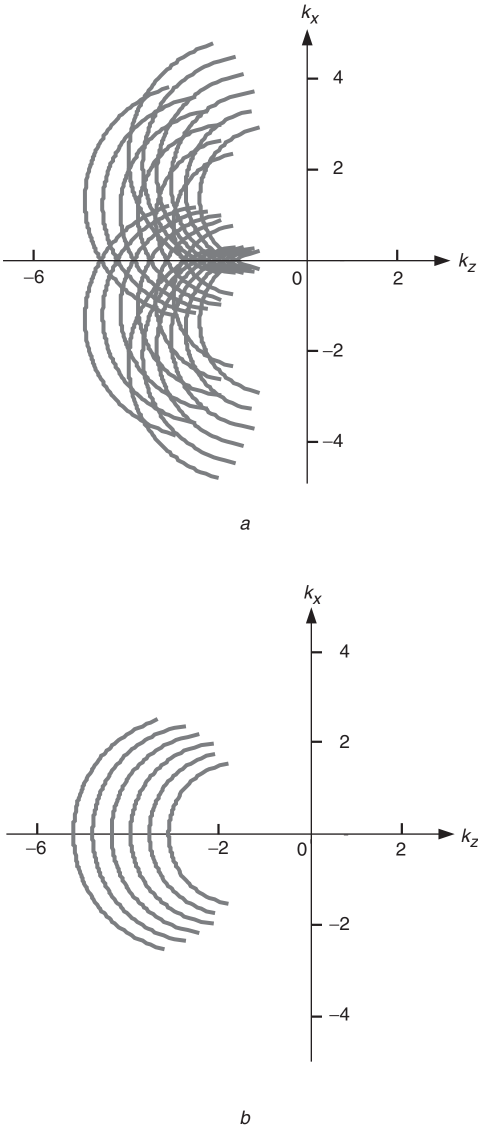

Fig. 5 *Fourier-domain acquired in the bistatic scattering arrangement*
a Four-source illumination at 60°, 30°, −30° and −60°
b Single-source illumination at 0°

(i) Measure the room clutter response using a linear scanner for all the measurement states.

(ii) Position the reference object and measure the scattered fields in all measurement states, then perform a one-dimensional Fourier transformation after subtracting room clutter response for each measurement state.

(iii) Locate the test object and measure the scattered fields in all measurement states. Calibrate the object Fourier-domain data using (15), then extract its corresponding Fourier-domain data using (20).

(iv) Use the triangle-based nearest neighbour interpolation method [20] to acquire the extracted Fourier-domain data from each illumination source in a rectangular format, then superpose all the Fourier-domain data. Finally, perform a two-dimensional inverse FFT to reconstruct the image.

4 Experimental results

Based on the above described measurement system and calibration procedure, this Section presents the experimental

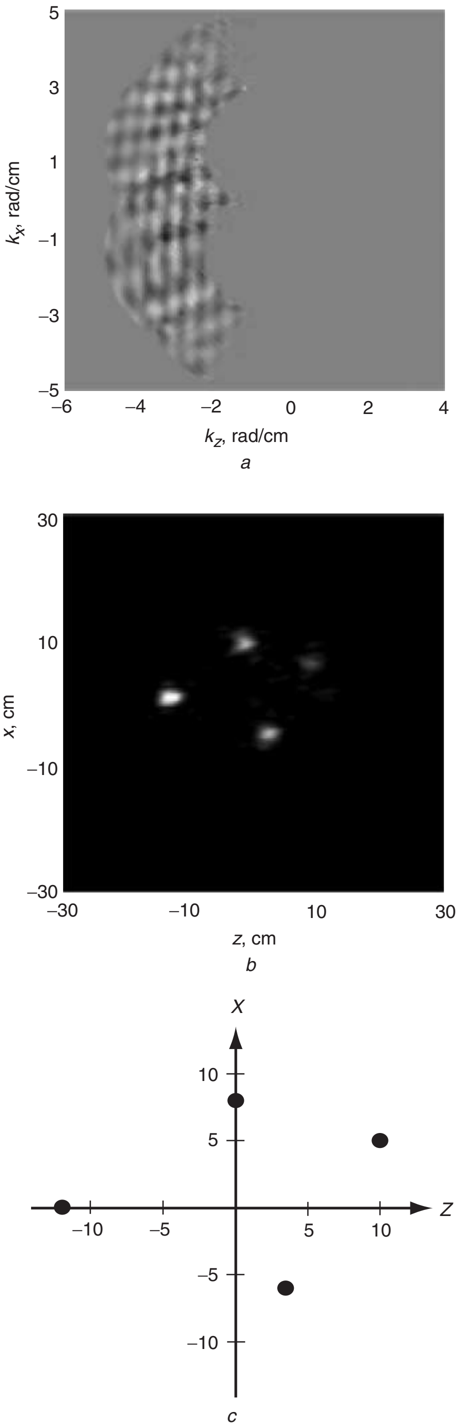

Fig. 6 *Measured results and the geometries of four thin cylinders*
a Fourier-domain data
b Reconstructed image
c Geometries of four thin cylinder at (−12, 0), (0, 8), (3.5, −6) and (10, 5) cm

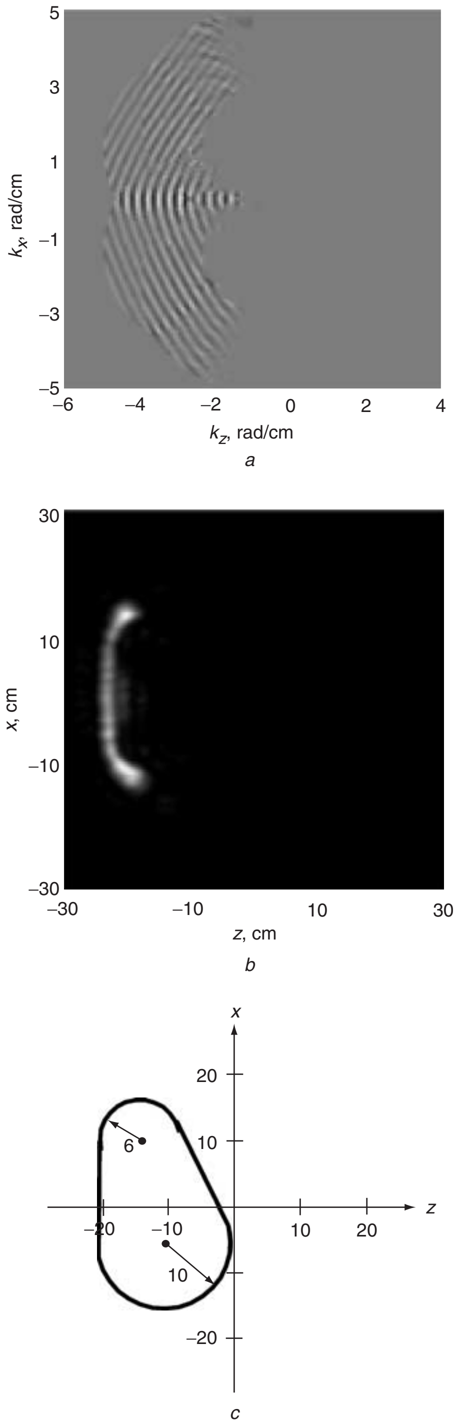

Fig. 7 *Measured results and the geometry of an egg-shaped metallic cylinder*
a Fourier-domain data
b Reconstructed image
c Scattering object geometry

results of four different types of scattering objects. They include a metallic cylinder with 91 cm length and 15 cm radius, four distributed metallic thin cylinders with 113 cm length and 1.5 cm radius as discrete line scatterers, a 91 cm long egg-shaped metallic cylinder having radii of curvature of 6 cm, 10 cm and infinity, and a metal covered B-52 1:100 scaled model aircraft.

In the measurement, the linear receiving array is synthesised by moving a WR-90 open-ended rectangular waveguide at 128 equally spaced positions. The frequency is stepped from 7.5 to 12.5 GHz for 51 frequency points. The stepping interval of linear scanner and frequency points satisfy the nonaliasing requirements [14]. A metallic cylinder with 91 cm length and 12.5 cm radius is used as a reference object.

For the test object of a metallic cylinder with 15 cm radius, the range of ka is 23.6–39.3 rad, hence the measurement is in physical optics regime. The measured Fourier-domain data shown in Fig. 3*a* is in good agreement with the simulation results given in Fig. 3*b*. Figure 4 shows the reconstructed images obtained from Fourier-domain data given in Figs. 3*a* and 3*b*, respectively. It is indicated that the reconstructed image shown in Fig. 4*a* gives about a 140° circular ring image corresponding to the shape of the

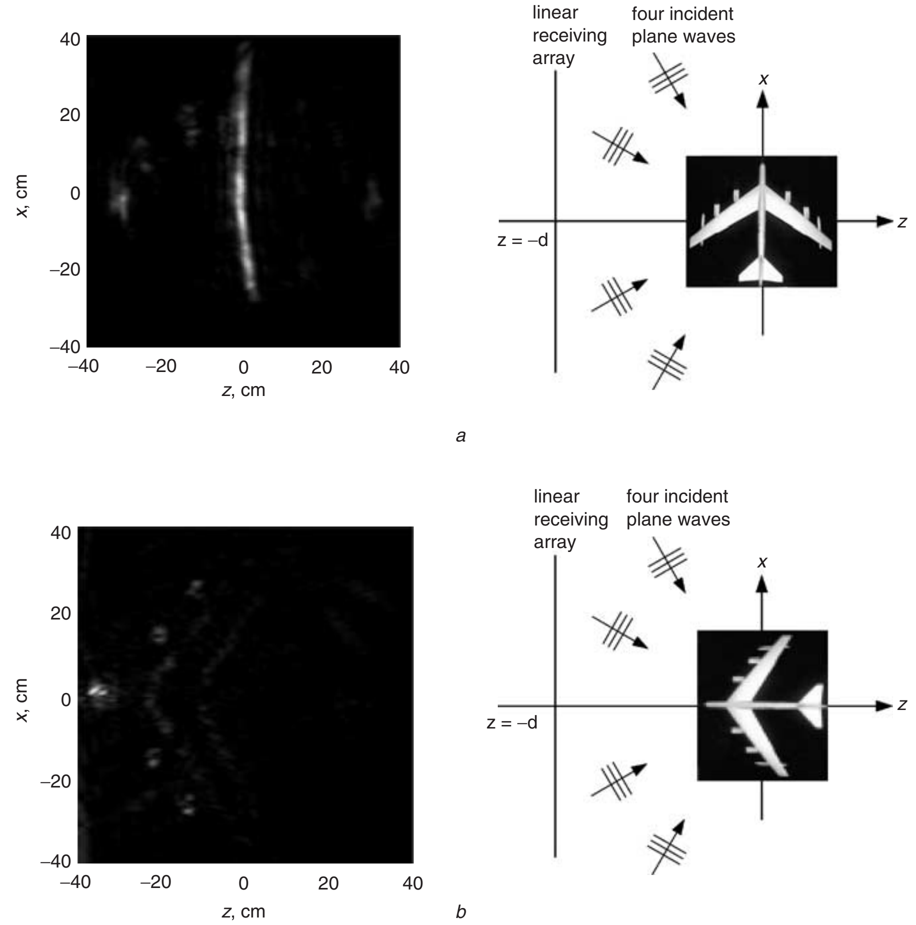

Fig. 8 *Reconstructed images and scattering arrangements of a B-52 1:100 scaled model aircraft*
a Side-view results
b Front-view results

metallic cylinder owing to the specular diffraction observed by the linear array under four-source illumination.

Figure 5*a* illustrates the Fourier-domain acquired by four-source illumination based on (6) and (10). The boundaries are about $-4\,\text{rad/cm} < k_x < 4\,\text{rad/cm}$ and $-5\,\text{rad/cm} < k_z < -2\,\text{rad/cm}$. The corresponding resolution then gives about 0.8 cm in the *x*-direction (or cross-range resolution) and 2 cm in the *z*-direction (or range resolution).

The use of the four-source illumination distributed at 60°, 30°, $-30°$ and $-60°$ in Fig. 2 is because this arrangement can effectively give about 140° Fourier-domain range with reasonably small overlapped regions. One can increase the Fourier-domain angular range to the limit of 180° by properly enlarging the distribution of the illumination source and receiving array. This will then yield to the limit 180° of object aspect angle. Note, a sparser source distribution may cause more empty areas in the Fourier domain.

In comparison, Fig. 5*b* shows the Fourier domain acquired by single-source illumination at 0°. Note that the Fourier-domain in Fig. 5*a* is about two to three times enlarged in the k_x-direction by using multisource illumination. Therefore, the microwave imaging system described in Section 3 is shown to be an effective approach to improve the object aspect angle and cross-range resolution by extending the area of induced surface current distribution using multisource illumination.

For the second type of test object, the range of *ka* is 2.4–3.9 rad, hence the thin cylinders can be treated as four line scatterers. Measured results of Fourier-domain data and reconstructed images are shown in Figs. 6*a* and 6*b*. The reconstructed image is shown to be in good agreement with the distribution of four thin cylinders given in Fig. 6*c*.

Note that the transmitting and receiving antennas are in the negative *z*-direction, hence the thin cylinder at (10, 5) cm is the furthest one. This cylinder is also under the partial blockage of the incident fields by the other three cylinders. Therefore, the reconstructed four images are shown relatively faintly along the positive *z*-direction.

The third type of test object is an egg-shaped metallic cylinder with three different curvatures. Measured results of Fourier-domain data and the reconstructed image are shown in Figs. 7*a* and 7*b*. Since the measurement system can provide about 140° object aspect angle, three different curvatures of the scattering object can be clearly distinguished from the reconstructed image. The fourth test object, a B-52 scaled aircraft, consists of continuous and discrete scattering centers. They are shown clearly in the reconstructed images of Figs. 8*a* and 8*b*. Note that the curved aircraft body can be identified from the side-view image owing to the wide object aspect angle, whereas the two twin engines on each wing can be differentiated in the front-view image because of the improvement of cross-range resolution.

5 Conclusions

In this paper, formulation, measurement system and calibration procedure for the microwave diversity imaging of conducting objects using multisource illumination are presented. They are used to extract the calibrated object Fourier-domain data from the measured scattered field in a backward scattering arrangement with multisource illumination.

The experimental results demonstrate that the developed microwave diversity imaging system using a multisource illumination arrangement can yield images with a wide object aspect angle and better cross-range resolution than those using a single-source illumination arrangement. This improvement is achieved by applying multisource illumination to extend the area of the induced surface current distribution on the scattering object and the boundaries of Fourier-domain data in the cross-range direction.

The developed microwave diversity imaging system using multisource illumination is demonstrated to have the potential as an effective approach in imaging radar, remote sensing and nondestructive evaluation.

6 Acknowledgments

This work was supported under the National Science Council and Ministry of Education of Taiwan, R.O.C. under Grants NSC 91-2219-E-002-030 and 89-E-FA06-2-4.

7 References

1 Lewis, R.M.: 'Physical optics inverse diffraction', *IEEE Trans. Antennas Propag.*, 1969, **17**, pp. 308–314

2 Bojarski, N.N.: 'A survey of physical optics inverse scattering identity', *IEEE Trans. Antennas Propag.*, 1982, **30**, pp. 980–989

3 Ausherman, D.A., Kozma, A., Walker, J.L., Jones, H.M., and Poggio, E.C.: 'Developments in radar imaging', *IEEE Trans. Aerosp. Electon. Syst.*, 1984, **20**, pp. 363–400

4 Chen, C.C., and Andrews, H.C.: 'Multifrequency imaging of radar turntable data', *IEEE Trans. Aerosp. Electon. Syst.*, 1980, **16**, pp. 15–22

5 Mensa, D.L.: 'High resolution radar imaging' (Artech House, Dedham MA, USA, 1981)

6 Tomiyasu, K.: 'Tutorial review of synthetic-aperture radar (SAR) with applications to imaging of the ocean surface', *Proc. IEEE*, 1978, **66**, pp. 563–584

7 Elachi, C., Bicknell, T., Jordan, R. L., and Wu, C.: 'Spaceborne synthetic-aperture imaging radars: applications, techniques and technology', *Proc. IEEE*, 1982, **70**, (10), pp. 1174–1209

8 Adams, M.F., and Anderson, A.P.: 'Synthetic aperture tomographic (SAT) imaging for microwave diagnostics', *Proc. IEEE*, 1982, **129**, pp. 83–88

9 Ozdemir, C., Bhalla, R., Trintinalia, L.C., and Ling, H.: 'ASAR-antenna synthetic aperture radar imaging', *IEEE Trans. Antennas Propag.*, 1998, **46**, pp. 1845–1852

10 Rahmat-Samii, Y., and Lemanczyk, J.: 'Application of spherical near-field measurements to microwave holographic diagnosis of antennas', *IEEE Trans. Antennas Propag.*, 1988, **36**, pp. 869–878

11 Pichot, C., Jofre, L., Peronnet, G., and Bolomy, J.C.: 'Active microwave imaging of inhomogeneous bodies', *IEEE Trans. Antennas Propag.*, 1985, **33**, pp. 416–425

12 Bolomey, J.C., and Pichot, C.: 'Microwave tomography: from theory to practical imaging systems', *Int. J. Imaging Syst. Technol.*, 1990, **2**, pp. 144–156

13 Farhat, N.H.: 'Microwave diversity imaging and automated target identification based on models of neural networks', *Proc. IEEE*, 1989, **77**, pp. 670–681

14 Lin, D.B., and Chu, T.H.: 'Bistatic frequency-swept microwave imaging: principle, methodology and experimental results', *IEEE Trans. Microw. Theory Tech.*, 1993, **41**, pp. 855–861

15 Chen, F.C., and Chew, W.C.: 'Ultra-wideband radar imaging experiment for verifying super-resolution in nonlinear inverse scattering', *Proc. IEEE Antennas Propagat. Soc. Int. Symp. Dig.*, 1998, **2**, pp. 1284–1287

16 Chen, F.C., and Chew, W.C.: 'Code-division multiplexing and frequency-division multiplexing for nonlinear inverse scattering', *Proc. IEEE Antennas Propagat. Soc. Int. Symp. Dig.*, 1999, **3**, pp. 2128–2131

17 Harrington, R.F.: 'Time-harmonic electromagnetic fields' (McGraw–Hill, New York, 1961)

18 Wolf, E.: 'Three-dimensional structure determination of semi-transparent objects from holographic data', *Opt. Commun.*, 1969, **1**, pp. 153–156

19 Appel-Hansen, J.: 'The handbook of antenna design-antenna measurements' (Peregrinus, London, 1982), Vol. 1, Chap 8

20 Appet Hansen, J.: MATLAB 'The language of technical computing' (MathWorks, Natick, MA, 1996)